Toward correction-free 8Li(, n)11B data at the Gamow energy of explosive nucleosynthesis

M La Cognata, A del Zoppo, R Alba, S Cherubini, N Colonna, A Di Pietro, P Figuera, M Gulino, L Lamia, A Musumarra, et al.

Towards correction-free ^{8}Li(α,n)^{11}B data at the Gamow energy of explosive nucleosynthesis

M.La Cognata[1,2], A.Del Zoppo[1], R.Alba[1], S.Cherubini[1,2], N.Colonna[5], A.Di Pietro[1], P.Figuera[1], M.Gulino[1,2], L.Lamia[1], A.Musumarra[1,2], M.G.Pellegriti[1,4], R.G.Pizzone[1], C.Rolfs[3], S.Romano[1,2], C.Spitaleri[1,2], A.Tumino[1,6]

[1]INFN-Laboratori Nazionali del Sud, Via S.Sofia 62, I95123 Catania, Italy
[2]Dipartimento di Metodologie Fisiche e Chimiche per l'Ingegneria, Università di Catania, I95123 Catania, Italy
[3]Institut fur Physik mit Ionenstrahlen, Ruhr-Universitat Bochum, Bochum, Germany
[4]Dipartimento di Fisica e Astronomia, Università di Catania, I95123 Catania, Italy
[5]INFN-Sezione di Bari, Via Orabona 4, I70126 Bari, Italy
[6]Università Kore, Enna, Italy

E-mail: delzoppo@lns.infn.it

Abstract. The ^{8}Li+^{4}He $\rightarrow$ ^{11}B+n reaction inside the center of mass energy region $E_{cm} = 0.5 - 2.5$ MeV, corresponding to the temperature range $T_9 = 1 - 5$, is of relevant interest in the fields of nuclear cosmology and nuclear astrophysics. In the context of Big-Bang nucleosynthesis, it has been invoked to overcome the A=8 mass gap; in r-process nucleosynthesis, it is considered a candidate precursor of seed nuclei. In this experimental work, the cross section, summed over all ^{11}B final bound states, at the energy of 1.05 MeV in the center-of-mass system, is investigated by a correction-free projectile-correlated inclusive neutron measurement. The radioactive ^{8}Li beam delivered by the EXCYT facility at LNS-Catania is used to induce the inverse-kinematics reaction process. A zero-energy-threshold 4π detection system is used. Thanks to the improved experimental and analysis procedures, the result obtained in this work represents a strong argument to reopen the debate on the magnitude of the ^{8}Li$(\alpha, n)^{11}$B reaction rate in explosive astrophysical environments.

PACS numbers: 25.60.-t,26.30.-k,26.35.+c

1. Introduction

Observations extended over high-redshift very primitive astrophysical objects (quasars and distant galaxies, for instance) have shown evidence of a non-negligible abundance of heavy nuclides, ^{12}C and heavier ([1] and references therein). Such results might be explained if some heavy-element production has taken place during the Big Bang nucleosynthesis. For instance, in the inhomogeneous Big Bang scenario [2, 3, 4, 5] neutron-rich high-baryon-density regions formed where heavy-element production could have taken place primarily following the

^{1}H(n,γ)^{2}H(n,γ)^{3}H(^{2}H,n)^{4}He(^{3}H,γ)^{7}Li(n,γ)^{8}Li(^{4}He,n)^{11}B(n,γ)^{12}B(β^{-})^{12}C... chain [1, 2, 3, 4, 5, 6, 7]. Such a pathway transits through the zero-energy-threshold ^{8}Li+^{4}He $\rightarrow$ ^{11}B+n reaction involving the short lived ^{8}Li isotope, having $T_{\frac{1}{2}}$ =840 ms.

The ^{8}Li+^{4}He $\rightarrow$ ^{11}B+n reaction could also play a crucial role to constrain the physical conditions characterizing the r-process site [8, 9]. Indeed, the necessary presence of seed nuclei (in the mass range $70 < A < 120$, like e.g. the doubly magic ^{78}Ni), which are eventually burnt to heavier elements in fast neutron-capture reactions, could be obtained through $\alpha-$capture reactions beginning from the two chains [9, 10, 11, 12]: (a) ^{4}He$(\alpha n,\gamma)^{9}$Be$(\alpha,n)^{12}$C and (b) ^{4}He$(t,\gamma)^{7}$Li$(n,\gamma)^{8}$Li$(\alpha,n)^{11}$B. According to calculations in [9], the concurrence of path (b) would determine a factor 2 increase for the entropy of the astrophysical environment, compared with calculations assuming path (a) only.

The ^{8}Li$(\alpha,n)^{11}$B reaction has also proved of interest in the study of nuclear structure and nuclear reaction mechanisms. As it has been pointed out in [13], the selective feeding of high-excitation-energy ^{11}B levels can hardly be understood invoking selection rules only. Rather it seems to signal that the nuclear structure of the initial ^{12}B and of the final ^{11}B excited states play the most important role in determining the marked branching ratio non-uniformity. This might indicate a ^{12}B cluster structure (already suggested by the large α, t and ^{5}He spectroscopic factors [14]) close to the $2\alpha + t$ exotic structure of the final ^{11}B state [15].

For the interest of nuclear astrophysics the experimental value of the ^{8}Li+^{4}He $\rightarrow$ ^{11}B+n reaction cross section summed over all energetically open final states of ^{11}B is required. Available cross section data at center-of-mass (c.o.m.) energies of about 1 MeV range from about 100 mb to about 600 mb [16, 17, 18, 19, 20, 21, 22]. Consequently, a more accurate experimental determination of the ^{8}Li+^{4}He $\rightarrow$ ^{11}B+n reaction cross section is needed. In principle, such a goal might be reached by either ^{11}B or neutron inclusive measurements. In this work the inclusive neutron measurement problem is addressed. In particular, we report on the improved determination of the cross section at 1.05 ± 0.16 MeV in the c.o.m system, corresponding to $T_9 \sim 2$. The experiment strategy is the one successfully adopted in our recent works [16, 18, 23, 13]. This is implemented here with complementary key experimental data and with the original development of the appropriate experiment formalism, to provide a more accurate estimate of the reaction cross section and to further support the reliability of both statistical and systematic uncertainties. Moreover, the cross section determination approach, which is exhaustively discussed in this work, might represent an useful tool for the study of nuclear structure and reactions between light halo systems.

The inverse-kinematics reaction induced by available low-intensity ^{8}Li beams on a ^{4}He gas-target is at present the only practicable approach because of the short ^{8}Li half life. Nonetheless, the notation ^{8}Li(α,n)^{11}B, which is proper of the direct kinematics, will be used in the following because is the most commonly cited one. This is the first in the series of measurements of this reaction planned at the EXCYT radioactive ion beam facility at Laboratori Nazionali del Sud (LNS) in Catania. Preliminary results and analysis of the present experiment have been presented in [18, 23].

2. The experiment set-up

The ^{8}Li beam was delivered by the EXCYT ISOL facility at Laboratori Nazionali del Sud in Catania. It was produced by injecting a $^{13}C^{4+}$ primary beam of 45 MeV/amu on a graphite target. After a 1/20000 isotopic purification, the beam was re-accelerated at the laboratory kinetic energy of about 11 MeV and transported to the ^{4}He gas-target of this experiment. This consisted of a (4 cm diameter, 15 cm long) cylindrical cell connected to the end of the beam pipe through a ~ 5 μm thick Ni entrance window. The pressure of 150 mbar was used. A beam stopper consisting in a thick tantalum disk was located at the end of the gas cell. The Ni window also acted as beam energy degrader. Two micro-channel-plate detectors (MCP1 and MCP2) were located upstream along the beam pipe, at 150 cm and 50 cm from the Ni entrance window, respectively. A removable silicon detector measured the ^{8}Li kinetic energy spectrum as a function of the depth z along the ^{4}He filled cell. The neutrons were detected using the Polycube thermalization counter [23, 24]. With its 4π geometry the detector integrates the neutron yield over the angular distributions. It consists of 12 cylindrical proportional counters (radius=1.27 cm and length=50 cm) filled with ^{3}He at the pressure of 4 atm which play the role of thermal neutron absorber. The 12 counters are embedded into a 40cm $\times$ 40cm $\times$ 40cm polyethylene moderator where fast neutrons are slowed down to thermal energies. The moderator is surrounded by a 0.6 mm thick cadmium shielding and by a 4π passive layer of polyethylene. The 12 ^{3}He counters are located parallel to a 11cm $\times$ 13cm $\times$ 40cm empty channel through the Polycube center that allows for the insertion of the beam pipe and of the ^{4}He gas-cell reaction chamber.

3. Beam purity and energy resolution inside the target cell

The 100% nominal beam purity of EXCYT was checked to persist at the target position. Fig. 1 shows the MCP1 to MCP2 time of flight versus the ^{8}Li kinetic energy at the cell entrance (depth $z = 0$ inside the gas-cell). This data supports the absence of beam contaminants to within the conservative upper limit of 1/10000.

Fig. 2 shows the ^{8}Li kinetic energy spectrum data for the two extreme cases $z = 0$ and $z = 15$ cm (end of the cell) along the ^{4}He filled cell. The mean ^{8}Li laboratory energy was $E_0 = 3.97$ MeV and $E_{15} = 2.43$ MeV. The nearly Gaussian energy dispersion, having almost constant variance square root value ($\delta E \approx 0.19$ MeV), reflected almost exclusively the energy straggling through the Ni entrance window. By integrating over the depth z, the resulting energy spectrum had a rectangular like shape with semi-gaussian rounded edges. The resulting variance square root was $[(E_0 - E_{15})^2/12 + \delta E^2]^{\frac{1}{2}} = 0.48$ MeV. In the c.o.m of the ^{8}Li+^{4}He reaction, the central value and the resolution were $E_{cm} = 1.05$ MeV and $\delta E_{cm} = 0.16$ MeV, respectively.

Fig. 2 also evidences that the beam energy upper tail in the gas cell was well below the energy threshold (6.1 MeV) of the ^{8}Li+^{4}He $\rightarrow$ ^{7}Li+^{4}He+n projectile break-up reaction and this ensures that the ^{11}B+n was the only open neutron production

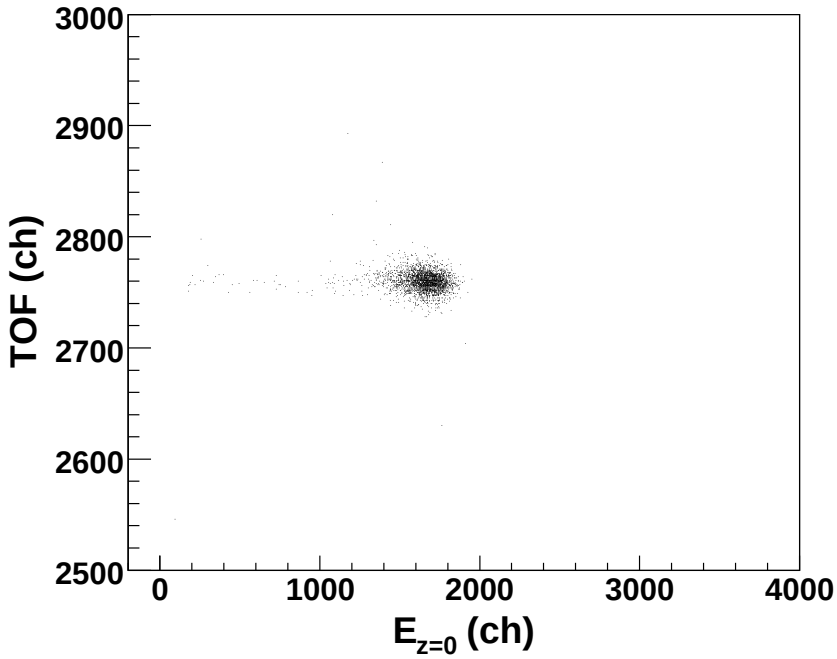

Figure 1. MCP1-MCP2 time of flight versus the ^{8}Li kinetic energy emerging from the Ni window.

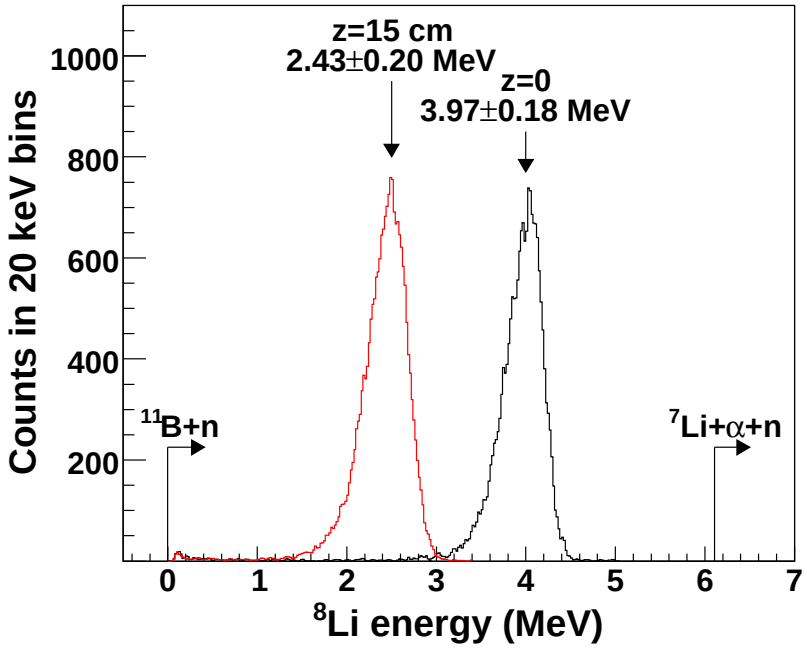

Figure 2. ^{8}Li energy profiles at the entrance ($z = 0$) and at the end ($z = 15$ cm) of the gas cell filled with ^{4}He at the pressure of 150 mbar. The arrows evidence the energy threshold of the lowest neutron producing channels in the ^{8}Li+^{4}He collisions.

channel of the present ^{8}Li+^{4}He reaction measurement.

4. Experiment strategy

The quintessential element of the present approach is the measurement of the time elapsed between the instant t_0 at which a ^{8}Li projectile impinges on the ^{4}He target nucleus and the instant $t_0 + t_{capt}$, at which the possibly produced reaction neutron is captured in the Polycube. The probability density of the neutron life t_{capt} inside the counter is given by the superposition of two exponentially decreasing components

$$\frac{dP_{nc}}{dt_{capt}} = \frac{q}{\tau_{fast}} e^{-\frac{t_{capt}}{\tau_{fast}}} + \frac{(1-q)}{\tau_{slow}} e^{-\frac{t_{capt}}{\tau_{slow}}} . \quad (1)$$

These follow from the presence of mainly two weakly absorbing media, polyethylene and air in the almost empty central channel, which determine different migration paths and lives of the thermalised neutrons before being captured in ^{3}He, the smaller the mean density along the migration path, the longer the capture time scale [23]. The values of the parameters $\tau_{fast} = 69 \pm 0.4\mu s$, $\tau_{slow} = 160 \pm 0.7\mu s$ and $q = 0.58 \pm 0.003$ [18, 23] are independent of the neutron energy in the $0.1 \div 20$ MeV range. The linear relation

$$\frac{1}{D_{tar}} \frac{1}{N_{proj}^{DT}} \frac{dn}{dt_{capt}} = \sigma \cdot \Omega \cdot \frac{dP_{nc}}{dt_{capt}} + b \quad (2)$$

occurring with the experimental differential neutron yield $\frac{dn}{dt_{capt}}$ determines the requested cross section σ. In Eq.2, b is the uncorrelated background level; D_{tar} is the target areal density; N_{proj}^{DT} is the total number of projectiles processed by the non-extending dead-time counting system used in this work; Ω is the neutron detector efficiency averaged over the laboratory neutron-energy spectrum associated to each energetically open ^{11}B level, as well as over the branching ratios for the feeding of these ^{11}B levels. Such a projectile-correlated experimental method allows to suppress most of the ambiguities otherwise connected to a purely inclusive neutron-counting approach. In particular, as indicated by Eq. 2, the projectile-correlated reaction neutrons can be unequivocally identified and separated from the unavoidable neutron(-like) uncorrelated background.

5. The measurements

The experiment consisted of the three types of measurements:
- a measurement without beam (Sec. 7.1);
- a set of projectile correlated measurements without ^{4}He (Sec. 7.2);
- a set of projectile correlated measurements with ^{4}He (Sec. 7.3).

In all cases the neutron capture instant was obtained by the OR of the 12 proportional counter logic outputs. The corresponding 12 pulse height spectra were also measured and recorded. In both projectile-correlated neutron-capture-time measurement types (with and without ^{4}He), the instant t_0 at which a projectile nucleus impinged on the target nucleus was signaled by its transit through the micro-channel-plate detector MCP2‡. The resulting signal was gated by a 10 ns wide window, generated by MCP1, centered at

‡ The micro-channel-plate detector MCP2 to target-center time of flight is of the order of only 30 ns.

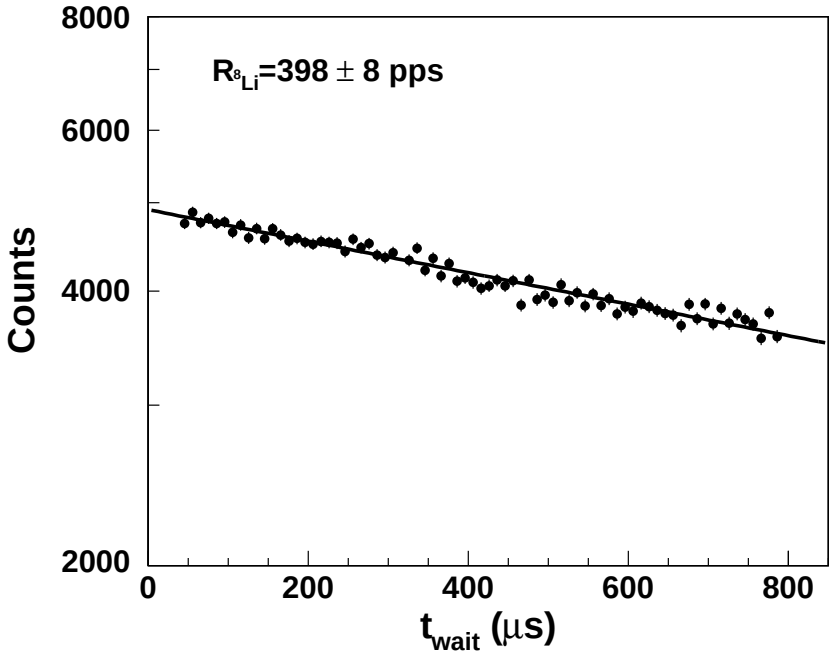

Figure 3. Experimental distribution of the waiting time between successive ^{8}Li arrival to the target. The fit according to the exponential dependence $c \cdot e^{-R_{^8Li} \cdot t_{wait}}$ (solid line) demonstrates the constancy of the projectile rate within a time scale as short as a sub-ms interval.

the peak of the MCP1 to MCP2 time of flight spectrum in Fig. 1 (FWHM=1.8 ns). The hardware of both MCPs was optimized as in [25] so as to get the same intrinsic efficiency value, very close to 100%. Dark counts of the individual MCP's were discarded by the requested MCP-MCP fast coincidence. Such a background-free t_0-device generated two main logic signals which provided the time-zero reference for two time-to-amplitude converters, one named TCAPT and the other named TWAIT:
- TCAPT was used to measure the distribution dn/dt_{capt} of the capture time t_{capt}.
- TWAIT was used to measure the distribution dN_{proj}/dt_{wait} of the waiting time t_{wait} between successive projectile arrivals to the target.
All projectile correlated measurements were performed at fixed dead time $DT = 1.1$ ms.

6. Dead-time-distorted beam stochasticity

In both types of measurement with ^{8}Li beam, with or without ^{4}He, runs using different projectile rate R_{proj} in the range (2-4)$\cdot 10^{-4}$ μs^{-1}, that is (200-400) pps, were performed. To investigate the beam stochasticity dependence on the dead time, the shape of the measured distribution dN_{proj}/dt_{wait} as a function of t_{wait} was considered. It is reported in Fig. 3. Its apparent exponentially decreasing dependence with increasing t_{wait} signals that in any arbitrary time interval of length Δt the t_0-counting device was exposed to

a poissonian source of projectiles with probability

$$P_{inc}(N_{proj}) = e^{-R_{proj}\cdot\Delta t}\,.\,\frac{(R_{proj}\cdot\Delta t)^{N_{proj}}}{N_{proj}!}\,. \tag{3}$$

In fact, for $\Delta t = t_{wait}$

$$\frac{dN_{proj}}{dt_{wait}} \propto P_{inc}(N_{proj}=0) = e^{-R_{proj}\cdot t_{wait}}. \tag{4}$$

In such a case, the distortions due to the dead time DT of the counting system in the statistics of the triggering projectiles can be calculated as in [26], the number N_{proj}^{DT} counted during the time interval Δt being regulated by the probability distribution

$$P(N_{proj}^{DT}) = \frac{\gamma[N_{proj}^{DT}, R_{proj}\cdot(\Delta t - N_{proj}^{DT}\cdot DT)]}{(N_{proj}^{DT}-1)!}$$
$$-\frac{\gamma\{(N_{proj}^{DT}+1), R_{proj}\cdot[\Delta t - (N_{proj}^{DT}+1)\cdot DT]\}}{N_{proj}^{DT}!}, \tag{5}$$

where $\gamma(j,x)$ is the incomplete gamma function [27]. The mean number of triggering projectiles and the variance-to-mean ratio are, respectively,

$$< N_{proj}^{DT} >= \frac{< N_{proj} >}{1 + R_{proj}\cdot DT} \tag{6}$$

$$\frac{\delta^2_{N_{proj}^{DT}}}{< N_{proj}^{DT} >} = \frac{1}{(1+R_{proj}\cdot DT)^2}. \tag{7}$$

Therefore, not only the mean number of accepted events $N_{proj}^{DT} < N_{proj}$ but also the statistics of accepted events substantially deviates from the poissonian behavior of the incident projectiles N_{proj} established in Fig. 3. In the present case, the variance-to-mean ratio (Eq. 7) ranges between 0.5 and 0.7, namely the distribution Eq.5 is significantly sub-poissonian. In the following, such an information will be used to check the statistical homogeneity of all sources which contribute to the inclusive $\frac{dn}{dt_{capt}}$ requested by Eq. 2.

7. Data sorting, analysis and results

The pulse height spectrum from each of the 12 ^{3}He-filled detector tubes is practically independent of the initial neutron energy. In fact, only after the thermalization in the Polycube moderator neutrons are detected through the $^{3}\mathrm{He}(n,p)^{3}\mathrm{H}$ capture reaction, having Q-value of 0.764 MeV and cross section of 5300 barns at $E_n = 0.025$ eV. Such a characteristic pulse height spectrum is shown in Fig. 4.

The prominent peak corresponds to the complete Q-value deposition in ^{3}He. With decreasing pulse height, the tail corresponds to progressively incomplete Q-value deposition in ^{3}He. The low energy tail edge, at pulse height $\equiv Q/4$, is due to neutrons captured near the counter wall with the proton depositing all of its energy in the wall.

The rejection of the nonphysical events, located inside the hatched areas illustrated in Fig. 4, is the only step of the off-line data sorting of the present experiment. Moreover, since in such a step only nonphysical events are rejected, no type of corrections is correspondingly requested in the subsequent data analysis.

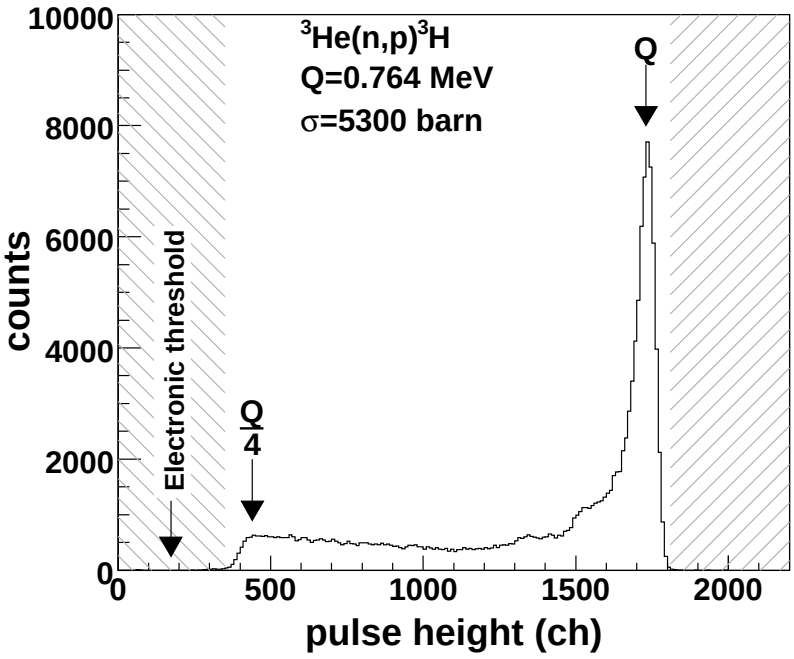

Figure 4. Characteristic pulse height spectrum of each of the 12 ^{3}He-filled detector tubes. The hatched areas emphasize the nonphysical pulse height regions

7.1. Measurement without beam

By allowing the Polycube to operate in single mode, the neutron-like count rate $R_{nat} = (3.3 \pm 0.05) \cdot 10^{-8}$ counts$\cdot\mu s^{-1}$ was observed. This natural background is almost exclusively due to α-emitting nuclides in the stainless steel housing of the ^{3}He proportional counters. The free background statistics is obviously poissonian, so that the probability of being in coincidence with a triggering projectile is $r = 1 - \exp(-R_{nat} \cdot t_{capt}^{max}) \approx 2.5 \cdot 10^{-5}$, $t_{capt}^{max} = 800\mu$s being the TCAPT range. Accordingly,

$$\psi(n) = \sum_{N_{proj}^{DT}} P_{DT}(N_{proj}^{DT}) \begin{pmatrix} N_{proj}^{DT} \\ n \end{pmatrix} r^n (1-r)^{(N_{proj}^{DT}-n)} \tag{8}$$

is the probability of observing n background signals, where $P_{DT}(N_{proj}^{DT})$ is the dead time distorted distribution Eq. 5. The corresponding variance-to-mean ratio

$$\frac{\delta_n^2}{< n >} = 1 - r \cdot \left(1 - \frac{\delta_{N_{proj}^{DT}}^2}{< N_{proj}^{DT} >}\right) \tag{9}$$

is not distorted by the dead time because $r \ll 1$.

Using this measured rate R_{nat}, we calculated the contribution to the constant b in Eq.4 as $10^{27} \cdot R_{nat} \cdot D_{^4He}^{-1}$. Following Eq. 2, this is reported in Fig. 5 as a function of the Polycube capture time probability density (Eq. 1).

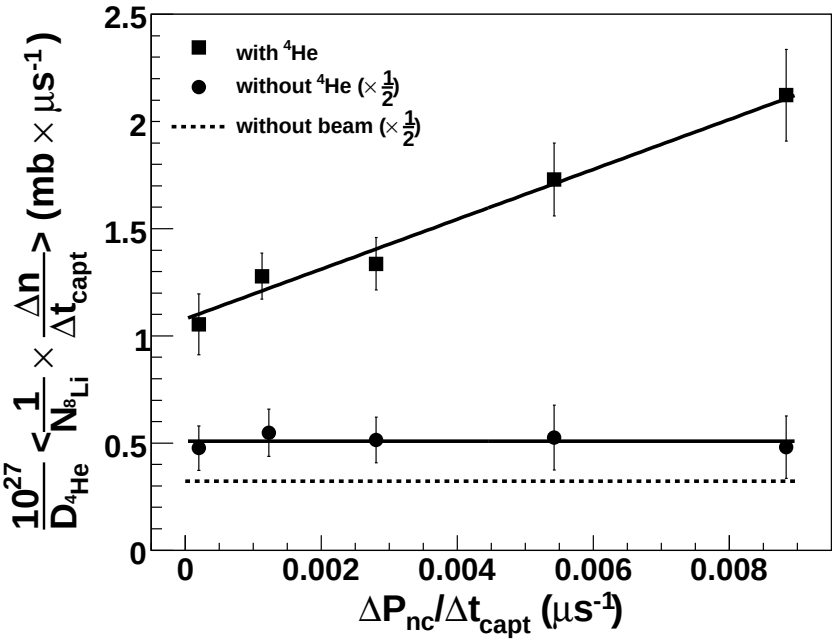

Figure 5. Experimental capture-time distributions as functions of the probability density (Eq. 1) from the measurement without beam (dots), without ^{4}He (filled circles) and with ^{4}He (filled squares). The statistical uncertainty only is shown.

7.2. Measurement without ^{4}He target

At the laboratory beam energy of this work, collisions with Ni or Ta nuclei at the beginning and at end of the gas cell, respectively, though below the corresponding Coulomb barrier heights, occur above the corresponding break-up thresholds of the weakly bound ^{8}Li nucleus into ^{7}Li+n. Such a break-up neutron contribution is correlated with the t_0-detector signal. Moreover, it exhibits the same linear dependence given by Eq. 2 with the slope determined by the $^8\mathrm{Li}(\alpha,n)^{11}$B-equivalent summed break-up mean cross section $\Sigma_x < \sigma_{b-u,x} > \cdot D_x \cdot D_{^4He}^{-1}$. Here, the brackets denote the average over the effective $x-$material thickness D_x, $x \equiv$ Ni,Ta and D_x is the effective thickness. The major contribution is due to ^{8}Li break-up on ^{58}Ni since the smaller ^{8}Li energy at the end of the gas target, the higher Ta charge and the thinner Ta effective thickness D_{Ta} suppress the equivalent cross section. No ^{8}Li+^{58}Ni break-up data is presently available. Therefore, an abundant overestimate of such a possible contamination was preliminarily determined by considering the available reaction cross sections for the non-halo medium-light systems ^{6}Li-^{7}Be+^{58}Ni [28], ^{6,7}Li-^{9}Be+^{64}Zn [29] and ^{6,7}Li+^{59}Co [30]. Following the recommendation by [31], these data were referred to ^{8}Li+^{58}Ni by dividing the c.o.m energies and the cross section values by the barrier heights $Z_1Z_2/(A_1^{1/3}+A_2^{1/3})$ and by the geometric factors $(A_1^{1/3}+A_2^{1/3})^2$, respectively, and multiplying by the corresponding factors of the ^{8}Li+^{58}Ni system. To further enforce the phenomenology, the ^{8}Li+^{208}Pb total reaction data of [32] has been also considered. Fig. 6 shows that the resulting

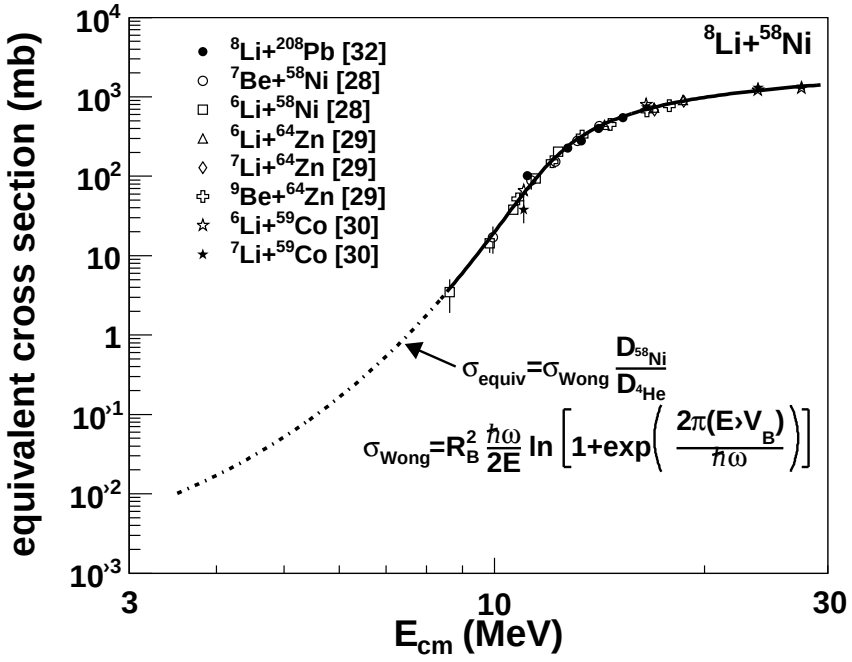

Figure 6. Upper limit of $^{8}\mathrm{Li}(\alpha,n)^{11}\mathrm{B}$-equivalent cross section associated to the projectile break-up reaction $^{8}\mathrm{Li}\rightarrow{}^{7}\mathrm{Li}+n$ on ^{58}Ni nuclei in the degrader, deduced from the total cross section of the indicated reactions (symbols), as a function of the c.o.m. energy of the $^{8}\mathrm{Li}+^{58}\mathrm{Ni}$ reference reaction. The solid line is the data fit by the Wong formula [33], with barrier curvature $\hbar\omega = 4.7 \pm 0.26$ MeV, height $V_B = 11.6 \pm 0.10$ MeV and radius $R_B = 9.53 \pm 0.14$ fm. The extrapolated dot-dashed low-energy tail emphasizes the upper limit in the E_{cm}-region of interest in this work (3.5-8.8 MeV).

$\sigma_{tot,\mathrm{Ni}} \cdot D_{Ni} \cdot D_{^4\mathrm{He}}^{-1}$ and, *a fortiori*, the break-up equivalent cross section on Ni do not exceed 4 mb in the c.o.m. energy range of interest in this work (3.5-8.8 MeV). The solid curve in Fig. 6 is the data fit using the Wong formula [33]. Its extrapolation (dot-dashed curve) allowed us to evaluate the realistic upper limit of about 1 mb for the mean equivalent total cross section. This represents a negligible systematic increase of the $^{8}\mathrm{Li}(\alpha,n)^{11}\mathrm{B}$ cross section value, expected in the range $100-600$ mb at $E_{cm} = 1.05$ MeV [16, 17, 18, 19, 20, 21, 22].

The measurement without ^{4}He was then performed to exclude the existence of additional, *a-priori* unexpected, strong correlated background contributions attributable to the beam transit nearby and/or inside the gas target cell. The energy loss of ^{8}Li in the ^{4}He gas along the whole projectile path to the tantalum disk was simulated by filling the target cell with Xe at the pressure of 22 mbar. The estimated contribution of the ^{8}Li break-up on Xe is well below 1 mb, as in the case of the tantalum beam stopper. The sorted data was treated as in the left hand side of Eq. 2. Fig. 5 shows that the capture time differential distribution measured without ^{4}He (filled circles) is independent of the Polycube probability density (Eq. 1).

This data is consistent with the total absence of strong projectile-correlated neutron production from reactions induced on targets other than ^{4}He. From Fig.5 the amount of

in-beam background can be deduced by subtracting the natural background contribution (dotted line). This tells us that $R_{in-beam} < R_{nat}$ and that, similarly to the uncorrelated natural background, also the statistics of the in-beam background is not distorted by dead time as the corresponding $r \ll 1$ in Eq. 8.

Considering that the upper limits of the expected correlated-neutron contamination determined in Fig. 6 does not exceed 1%, no correction is correspondingly requested.

7.3. Measurement with ^{4}He target

The statistical behavior of the physically correlated events, in which the triggering t_0 and the reaction neutrons are generated by the same ^{8}Li projectile, is similar to the natural and in-beam background ones. It is poissonian as $r\Omega = D_{tar}\sigma\Omega$ equals at most $3.5 \cdot 10^{-5}$ (assuming $\sigma = 600$ mb and $\Omega = 1$). Consequently, the experimental $\frac{\Delta n}{\Delta t_{capt}}$ is the sum of three statistically homogeneous contributions, one physically correlated and the other two (natural and in-beam) not correlated with the triggering projectile.

The sorted data was treated as in the left hand side of Eq. 2. In particular, the arithmetic average over the set of the performed runs of the rate- and dead-time-independent $\frac{1}{N_{proj}^{DT}}\frac{\Delta n}{\Delta t_{capt}}$ experimental values was considered. The statistical uncertainties were propagated accordingly. The resulting differential neutron event distribution as a function of the Polycube capture time probability density (Eq. 1) is shown in Fig. 5.

Strikingly, the data follows the linear dependence expected for correlated neutron capture according to Eq. 2. As $^8\mathrm{Li} \rightarrow {}^7\mathrm{Li}{+}n$ break-up on ^{4}He is excluded by energy conservation (see Fig. 2), the slope is entirely attributed to the neutrons produced in the $^8\mathrm{Li}(\alpha, n)^{11}\mathrm{B}$ reaction. Moreover, Fig. 3 shows that significant non-statistical ^{8}Li-projectile rate fluctuations are absent even in the deep sub-millisecond time scale. This rules out any type of t_{capt}-correlated background, which might have been set in spurious coincidences between a triggering t_0 and a $^8\mathrm{Li}(\alpha, n)^{11}\mathrm{B}$ reaction neutron generated by a different projectile. Consequently, no correction is requested. Hence, the slope of the straight line in Fig. 5 determines the cross section according to Eq. 2.

The least square fit of the data obtained with ^{4}He target gives $\sigma \cdot \Omega = 116 \pm 25$ mb. It follows that $r\Omega = D_{tar} \cdot \sigma \cdot \Omega \sim 6 \cdot 10^{-6}$ fully justifies the adoption of Poisson statistics in the evaluation of the error bar of each data set in Fig. 5.

The spurious coincidences constitute an extra in-beam (plus target) uncorrelated background, which adds up to the natural and in-beam background. Altogether they solely contribute to the t_{capt}-independent background b in Eq. 2. The contribution of the extra in-beam (plus target) uncorrelated background depends on the incident beam rate and equals $R_{proj} \cdot \sigma \cdot \Omega \sim 0.04$ mb$\cdot\mu s^{-1}$. This is quite small in comparison with the other background contributions and is fully consistent with the observation that the fitted value of the constant $b = 1.08 \pm 0.09$ mb$\cdot\mu s^{-1}$ coincides, within the statistical uncertainty, with the result of the measurement without ^{4}He (filled circles in Fig. 5).

8. The recommended $^{8}\mathbf{Li}(\alpha, n)^{11}\mathbf{B}$ cross section value

The present inclusive neutron measurement provides the information

$$\sigma = \frac{116 \pm 25}{\Omega}\ mb \tag{10}$$

which determines the practically correction-free $^{8}\mathrm{Li}(\alpha, n)^{11}\mathrm{B}$ reaction cross section at $E_{cm} = 1.05 \pm 0.16$ MeV, because the only unavoidable correction concerns the detection efficiency, as it is usual in experimental physics.

Fig. 7 shows the Polycube efficiency measured with ^{252}Cf and AmBe sources placed at the detector center. In the laboratory neutron energy range of interest (left panel of Fig. 8), the data points in Fig. 7 from the two sources represent a valuable experimental reference for detailed Monte Carlo calculations. These were performed by implementing beam pipe and gas cell in the GEANT 3.21 code used in [18, 23]. Fig. 7 shows the resulting detection efficiency for mono-energetic, isotropic sources at rest in the laboratory frame (histogram). This is in excellent agreement with the source data points. To account for the reaction kinematics, the formation of the ^{12}B compound nucleus in the most likely entrance-channel angular momentum $l = 0$ was considered. Consequently, isotropic neutron emission in the c.o.m. was adopted for each of the involved ^{11}B levels (see, for instance, [34]). The initial beam energy spread, the beam energy loss inside the gas-cell and the range of the reaction point coordinate were also taken into account. The resulting set of detection efficiency values Ω_{level}, each averaged over the corresponding laboratory neutron energy spectrum is reported in Fig. 7. The detection efficiency Ω requested in Eq. 10 is the average of all Ω_{level}-values weighted by the $^{8}\mathrm{Li}(\alpha, n)^{11}\mathrm{B}$ reaction branching ratios f_{level}

$$\Omega = \sum f_{level} \cdot \Omega_{level}. \tag{11}$$

In Ref. [18] an uniform feeding of ^{11}B excited states has been adopted for simplicity. Two determinations of the branching ratio pattern are available in the literature: the one from [20], which result from an average extended over the broad $0.75 \leq E_{cm} \leq 2.55$ MeV range; the one in [13], deduced from the comparison of the inclusive data [16, 18, 35, 19] with the $n - ^{11}$B coincidence data in [20]. In Tab. 1, the resulting detection efficiencies (and the propagated uncertainties) evaluated accordingly are given together with the corresponding cross-section values calculated by means of Eq. 10 (and the related errors). The largest cross section $\sigma = 637 \pm 138$ mb is obtained if the branching ratios from [20] are assumed in Eq. 11. Indeed, a seemingly weak non-uniformity of the branching ratios privileges the lower excited levels of ^{11}B and, consequently, the smaller values of the detection efficiency Ω_{level} (see Fig. 7). On the other hand, the smallest cross section $\sigma = 516 \pm 111$ mb results if the branching ratio pattern from [13] is considered in Eq. 11. In this case, a significant branching ratio non-uniformity right at $E_{cm} = 1.05$ MeV privileges the higher excited levels of ^{11}B and, consequently, larger values of the detection efficiency Ω_{level} (see Fig. 7). The differences in Tab. 1 reflect the moderate Ω_{level} dependence on the final ^{11}B excitation energy. Though these differences are of the same order of the given uncertainty, since the branching ratio pattern at the

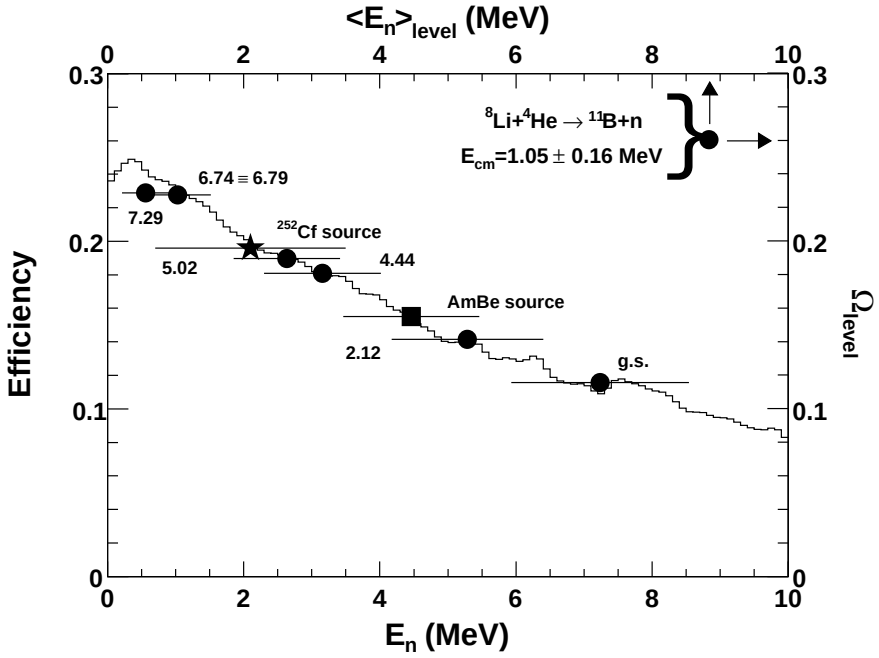

Figure 7. Polycube detection efficiency as measured in this work and in [24] using ^{252}Cf and AmBe sources (filled star and filled square, respectively). The histogram is the result of Monte Carlo calculations for mono-energetic neutrons from isotropic sources at rest. The filled circles result from Monte Carlo calculations for the ^{8}Li(α,n)^{11}B reaction neutrons for each of the energetically open levels of ^{11}B at $E_{cm} = 1.05 \pm 0.16$ MeV. The ^{11}B levels are labelled by their excitation energies (MeV). The effect of the c.o.m. motion is generally negligible, except at low energies where small deviations from the histogram are due to the increased forward escape along the detector central channel. Each horizontal bar shows the laboratory neutron energy spread. The statistical uncertainty of the shown simulations is typically about 0.7%.

Table 1. Detection efficiency (Eq. 11) and ^{8}Li$(\alpha, n)^{11}$B cross section (Eq. 10) at $E_{cm} = 1.05 \pm 0.16$ MeV for different branching ratio patterns.

Pattern	efficiency	cross section (mb)
uniform	$\Omega = 0.195 \pm 0.0005$	$\sigma = 594 \pm 128$
from Ref. [20]	$\Omega = 0.182 \pm 0.002$	$\sigma = 637 \pm 138$
from Ref. [13]	$\Omega = 0.225 \pm 0.002$	$\sigma = 516 \pm 111$

appropriate c.o.m. energy is available [13], we recommend $\sigma = 516 \pm 111$ mb as the ^{8}Li$(\alpha, n)^{11}$B cross section value at $E_{cm} = 1.05 \pm 0.16$ MeV.

9. Discussion

The present result is compared in Tab. 2 with the cross section values at the same c.o.m. energy from different experimental approaches.

First of all we briefly highlight the main features of these experimental procedures.

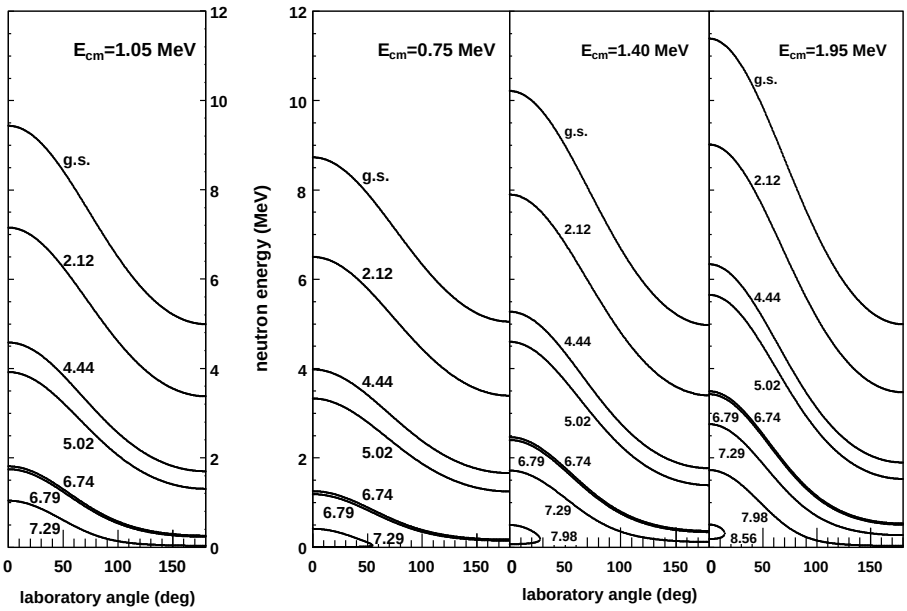

Figure 8. The laboratory energy ranges spanned by the $^{8}\mathrm{Li}(\alpha,n)^{11}\mathrm{B}$ reaction neutrons for each of the involved ^{11}B final states at the indicated E_{cm} values.

In the ^{11}B inclusive measurements [19, 35], an active target consisting of a multi sampling ionization chamber, the detector gas being mostly ^{4}He, was used. The resulting cross section is given in the second line of Tab. 2. The procedure to discriminate ambiguous events in such a ^{11}B inclusive measurement approach was criticized in [36]. To suppress such undistinguished contaminants, ^{11}B-n kinematical coincidence measurements were then introduced [20, 21, 22, 36]. A multiple-sampling and tracking proportional chamber surrounded by modular neutron counters consisting of plastic scintillators was used. The results at $E_{cm} = 1.05$ MeV by [20, 21, 22], obtained using the same set-up, are shown in Tab. 2. Such a variety of results, differing even by a factor 4.7, well outside the statistical uncertainty, demonstrates the complexity of such an approach.

In the present neutron-inclusive measurement, the background contribution has been carefully identified and evaluated. Since different sources of systematical uncertainties and of background are involved, the present data strongly confirms and supports the complementary ^{11}B inclusive data [19] in Tab. 2.

Opposite to the ^{11}B-n coincidence approach [20, 21, 22] we have shown in this work that a single, simple correction is required to extract the cross section, namely the one for detection efficiency in Eq. 10, and that all the possible sources of systematic uncertainties give a negligible contribution. The present new cross section value differs from the one in [18] by only about 10% thanks to the new improved data analysis performed here and, most importantly, to the effect of the new branching ratio pattern in [13]. It is also worth to underscore that by focusing on the cross section value recommended in [20] (Tab.2) by no means a factor of 5 difference with our result can

Table 2. Summary of the cross sections values as given in the listed references.

Measurement	Ref.	E_{cm} (MeV)	cross section (mb)	accuracy
n-inclusive	present work	1.05 ± 0.16	$\sigma = 516 \pm 111$	21.5%
^{11}B-inclusive	[19]	1.03 ± 0.07	$\sigma = 531 \pm 63$	12%
$n - {}^{11}$B	[21]	1.05 ± 0.05	$\sigma = 570 \pm 185$	32%
$n - {}^{11}$B	[22]	1.05 ± 0.05	$\sigma = 285 \pm 100$	35%
$n - {}^{11}$B	[20]	1.05 ± 0.05	$\sigma = 122.8 \pm 27.5$	22%

be recovered by radically changing the Polycube detection efficiency in Eq. 10 inside the range fixed by Fig. 7. As discussed in Ref. [13], in the study of the $^{8}\mathrm{Li}(\alpha, n)^{11}\mathrm{B}$ cross section the role of the detection threshold in determining the detection efficiency at low neutron energy is of fundamental importance. For the detector used in this work, the efficiency curve in Fig. 7 show how suited the Polycube design is to detect low energy neutrons. This makes the experimental setup more sensitive to high ^{11}B excited states yielding the lowest energy neutron as in the kinematics examples shown in Fig. 8. Conversely, in the measurements using plastic scintillators (as in [20]), which are typically characterized by a threshold of the order of 0.5 MeV, high ^{11}B excited states are experimentally unaccessible (Fig. 8, right panel) and the requested cross section summed over all ^{11}B final states cannot be measured.

10. Summary and conclusion

In this paper, we provide a thoroughly account of the neutron-inclusive measurement of the $^{8}\mathrm{Li}(\alpha, n)^{11}\mathrm{B}$ reaction cross section. In particular, we report on its improved determination by exhaustively analyzing the possible sources of systematic uncertainties and exploring the effect of the new branching ratio pattern [13].

The new determination of the $^{8}\mathrm{Li}(\alpha, n)^{11}\mathrm{B}$ cross section value $\sigma = 516 \pm 111$ mb turns out to be about 10% smaller than that given in our previous letter [18], while the effect of the sources of systematic uncertainties has proved to be negligible. The present experiment indisputably supports the complementary ^{11}B-inclusive measurement [19] at least at $E_{cm} = 1.05$ MeV. Both are in total disagreement with the recent $^{11}\mathrm{B}{-}n$ coincidence data [20]. The much larger (a factor ~ 5) cross section value measured here reopens the debate on the astrophysical consequences of the $^{8}\mathrm{Li}(\alpha, n)^{11}\mathrm{B}$ reaction.

In this framework, the correction-free inclusive approach discussed here can contribute to this debate by providing an accurate determination of the $^{8}\mathrm{Li}(\alpha, n)^{11}\mathrm{B}$ excitation function below the threshold of the $^{8}\mathrm{Li}{+}^{4}\mathrm{He} \rightarrow {}^{7}\mathrm{Li}{+}^{4}\mathrm{He}{+}n$ projectile break-up reaction ($E_{cm} = 2.03$ MeV). Indeed, the low-energy region (below 1 MeV) of the cross section might be crucial because possible resonances, due to ^{12}B unexplored excited levels [14], might enhance the reaction rate at the temperatures of interest for explosive nucleosynthesis ($T_9 = 1 - 5$). Since the mean capture time is $\overline{t_{capt}} = q \cdot \tau_{fast} + (1-q) \cdot \tau_{slow} \approx 110 \mu s$, measurements with intensities up to 10^4 ions/s ($\sim 25 - 50$

times larger than what used here) can be performed. Therefore, sufficient statistics can be easily collected to reduce the present measurement uncertainty at least by a factor 4-5. A conservative 20% accuracy can be reached even at $E_{cm} = 0.3$ MeV, where the cross section can be as low as 50 mb (extrapolating data in [19]).

This experimental technique may also represent an alternative approach for nuclear structure and reaction studies at low energies.

References

[1] Matsuura S et al. 2005 *Phys. Rev.* D **72** 123505
[2] Kajino T & Boyd R 1990 *Astrophys. J.* **359** 267
[3] Lara JF et al. 2006 *Phys. Rev.* D **73** 083501
[4] Malaney RA & Fowler WA 1988 *Astrophys. J.* **333** 14
[5] Rauscher T et al. 2007 *Phys. Rev.* D **75** 068301
[6] Witten E 1984 *Phys. Rev.* D **30** 272
[7] Applegate JH et al. *Phys. Rev.* D **35** 1151
[8] Sasaqui T et al. 2005 *Astrophys. J.* **634** 534
[9] Sasaqui T et al. 2006 *Astrophys. J.* **645** 1345
[10] Woosley SE & Hoffman RD 1992 *Astrophys. J.* **395** 202
[11] Hoffman RD et al. 1997 *Astrophys. J.* **482** 951
[12] Terasawa M et al. 2001 *Astrophys. J.* **562** 470
[13] La Cognata M et al. 2009 *Astrophys. Journal Lett.* **706** L251
[14] Soic N et al. 2003 *Europhys. Lett.* **63** 524
[15] Kawabata T et al. 2007 *Phys. Lett.* B **646** 6
[16] Cherubini S et al. 2004 *Eur. Phys. J.* A **20** 355
[17] Agodi C et al. 2006 *Nucl. Instrum. Methods* A **565** 406
[18] La Cognata M et al. 2008 *Phys. Lett.* B **664** 157
[19] Gu X et al. 1995 *Phys. Lett.* B **343** 31
[20] Ishiyama H et al. 2006 *Phys. Lett.* B **640** 82
[21] Hashimoto T et al. 2004 *Nucl. Phys.* A **746** 330
[22] Miyatake H et al. 2004 *Nucl. Phys.* A **738** 401
[23] Del Zoppo A et al. 2007 *Nucl. Instrum. Methods* A **581** 783
[24] Wrean PR & Kavanagh RW 2000 *Phys. Rev.* C **62** 055805
[25] Musumarra A et al. 2010 *Nucl. Instrum. Methods* A **612** 399
[26] Carloni F et al. 1970 *Nucl. Instr. Meth.* **78** 70
[27] Abramowitz M & Stegun IA (eds) 1965 *Handbook of Mathematical Functions* (New York: Dover Publications)
[28] Aguilera EF et al. 2009 *Phys. Rev.* C **79** 021601
[29] Gomes PRS et al. 2005 *Phys. Rev.* C **71** 034608
[30] Beck C et al. 2007 *Phys. Rev.* C **75** 054605
[31] Gomes PRS et al. 2005 *Phys. Rev.* C **71** 017601
[32] Kolata JJ et al. 2002 *Phys. Rev.* C **65** 054616
[33] Wong CY 1973 *Phys. Rev. Lett.* **31** 766
[34] Evans RD 1969 *The Atomic Nucleus* (New York: McGraw-Hill)
[35] Boyd RN et al. 1992 *Phys. Rev. Lett.* **68** 1283
[36] Mizoi Y et al. 2000 *Phys. Rev.* C **62** 065801